

Banner appropriate to article type will appear here in typeset article

arXiv:2501.02121v1 [physics.flu-dyn] 3 Jan 2025

# Turbulence-Resolving Integral Simulations for Wall-Bounded Flows

Tanner Ragan<sup>1</sup>†, Mark Warnecke<sup>1</sup>‡, Samuel T. Stout<sup>1</sup>¶ and Perry L. Johnson<sup>1</sup>||

<sup>1</sup>University of California Irvine, Mechanical and Aerospace Engineering Department, Samueli School of Engineering, Irvine, CA, USA

(Received xx; revised xx; accepted xx)

The physical fidelity of turbulence models can significantly benefit from a partial resolution of fluctuations, but doing so often comes with a significant increase in computational cost. To explore this trade-off in the context of wall-bounded flows, this paper introduces a framework for Turbulence-Resolving Integral Simulations (TRIS) with the goal of efficiently resolving the largest motions using two-dimensional fields defined by instantaneous wall-normal integration of velocity and pressure. Self-sustaining turbulence with qualitatively realistic large-scale structures is demonstrated for TRIS on an open-channel (half-channel) flow using moment-of-momentum integral equations derived from Navier-Stokes with relatively simple closure approximations. Evidence from Direct Numerical Simulations (DNS) suggests that such an approach can resolve 35 – 40% of the Reynolds shear stress at arbitrarily high Reynolds number. The current implementation of TRIS can match this resolution while simulating one flow through time in  $\sim 1$  minute on a single processor, even for very large Reynolds number. The present proof-of-concept TRIS results shown here rely on parameter tuning, and some quantitative differences with DNS spectra are observed, motivating ongoing and future efforts towards physics-based closures as well as extension to more general flow configurations such as boundary layers on immersed objects.

## 1. Introduction

The wide range of scales involved in turbulent boundary layers and other forms of wall-bounded turbulence, common to many engineering and natural flows, presents a difficult challenge to computational modeling and prediction efforts (Spalart 2000; Goc *et al.* 2020; Yang & Griffin 2021). To summarize, the cost of Direct Numerical Simulations (DNS) rises rapidly with increasing Reynolds number, making its use for practical applications computationally infeasible for the foreseeable future. The Large-Eddy Simulation (LES) framework, meanwhile, provides a potential alternative, but cost savings in wall-resolved LES (WR-LES) remain minimal compared to DNS. Consequently, Reynolds-Averaged Navier-Stokes (RANS) models remain relevant and popular. Even with wall-modeled LES (WM-LES) or hybrid RANS-LES techniques, scale-resolving simulations can be costly (even prohibitively so) for turbulent boundary layers at large Reynolds number.

† Email address for correspondence: ragant@uci.edu

‡ Email address for correspondence: mwarneck@uci.edu

¶ Email address for correspondence: stoutst@uci.edu

|| Email address for correspondence: perry.johnson@uci.edu

RANS-based integral methods for turbulent boundary layers, which pre-date the explosion of computer performance over the past half-century (Kline *et al.* 1968), provide a significant reduction in computing cost by seeking a solution for (averaged) quantities integrated in the wall-normal direction across the turbulent boundary layer. For aerodynamic and hydrodynamic boundary layers over immersed bodies, integral methods can be coupled with potential flow solvers to provide rapid prediction, albeit at reduced physical fidelity, e.g., Drela (1989). The use of depth-averaged equations is similarly common in many other wall-bounded turbulence scenarios, e.g., Ungarish (2010).

Approaches that partially resolve turbulent fluctuations (e.g., LES) potentially offer a substantial advantage in physical fidelity (over their RANS-based counterparts) because of their inherent ability to capture nonlocal behavior in the large-scale motions (Guala *et al.* 2006). This paper explores the possibility of Turbulence-Resolving Integral Simulations (TRIS), that is, LES-like integral methods in which wall-normal integration is carried out across the entire turbulent layer thickness. By reducing the description of the turbulent flow from three to two dimensions, a significant cost savings is possible. At the outset, however, it is not clear (i) how much of the turbulence can still be captured in this two-dimensional (2D) representation, and (ii) how unsteady, 2D, Navier-Stokes-based evolution equations can be developed which support self-sustaining turbulence with realistic structure. This paper provides an answer for these two questions in the simplified context of an open-channel (half-channel) flow.

## 2. Instantaneous Moment-of-Momentum Evolution Equations

In this section, evolution equations for TRIS are derived from the Navier-Stokes equations and boundary conditions for an open-channel flow, a useful surrogate to capture general characteristics of boundary layer turbulence. This configuration allows the homogeneity in the wall-parallel direction to provide a simple starting point for developing the TRIS framework without the added complexities of spatial development and interaction with a potential flow.

To guide the derivation, the notation will distinguish between wall-normal and wall-parallel components. Using a 2D index notation, the indices correspond to the streamwise ( $i = 1$ ) and spanwise ( $i = 2$ ) directions, such that implied summation only applies over the wall-parallel directions. Therefore, the notation used here is  $u_1 = u$ ,  $u_2 = w$ , and  $v$  along with  $x_1 = x$ ,  $x_2 = z$ , and  $y$  for the streamwise, spanwise, and wall-normal components of velocity and position, respectively. The conservation equations for incompressible flow are non-dimensionalized by the height of the open-channel ( $h$ ) and friction velocity ( $u_\tau$ ). The bottom wall of the open-channel ( $y = 0$ ) is a no-slip, no-penetration boundary whereas a no-penetration, zero-vorticity boundary condition is applied at the top wall ( $y = 1$ ). Using this notation, the incompressible Navier-Stokes equations for conservation of mass, wall-parallel momentum and wall-normal momentum are,

$$\frac{\partial u_i}{\partial x_i} + \frac{\partial v}{\partial y} = 0, \quad (2.1)$$

$$\frac{\partial u_i}{\partial t} + \frac{\partial u_i u_j}{\partial x_j} + \frac{\partial u_i v}{\partial y} = -\frac{\partial p}{\partial x_i} + \frac{1}{Re_\tau} \left( \frac{\partial^2 u_i}{\partial x_j \partial x_j} + \frac{\partial^2 u_i}{\partial y^2} \right) + \delta_{i1}, \quad (2.2)$$

$$\frac{\partial v}{\partial t} + \frac{\partial v u_j}{\partial x_j} + \frac{\partial v v}{\partial y} = -\frac{\partial p}{\partial y} + \frac{1}{Re_\tau} \left( \frac{\partial^2 v}{\partial x_j \partial x_j} + \frac{\partial^2 v}{\partial y^2} \right). \quad (2.3)$$

Here,  $Re_\tau = \rho u_\tau h / \mu$  is the friction Reynolds number for a fluid with density  $\rho$  and viscosity

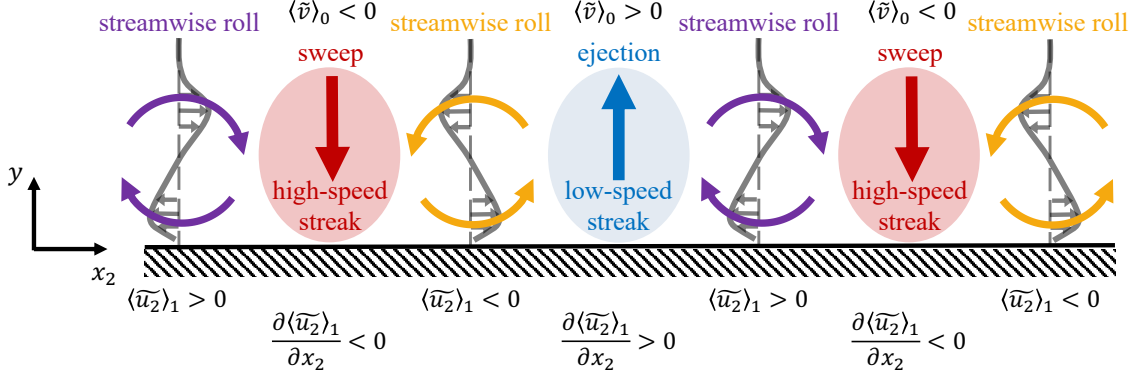


Figure 1: View in the flow direction of the large-scale streamwise rolls generating regions of high and low speed streaks, which correspond to sweeps and ejections, respectively. The profiles located at the streamwise rolls represent the local spanwise velocity. This phenomena encapsulates the effect of (2.5) (right).

$\mu$ .  $\delta_{i1}$  is the dimensionless imposed pressure gradient that drives the flow and  $p$  is the dimensionless pressure field that enforces (2.1).

Flow fields are integrated in the wall-normal direction and represented as zeroth and first moments, respectively,

$$\langle \phi \rangle_0(x_1, x_2, t) = \int_0^1 \phi(x_1, x_2, y, t) dy, \quad \langle \phi \rangle_1(x_1, x_2, t) = \int_0^1 2y \phi(x_1, x_2, y, t) dy. \quad (2.4)$$

Thus, the zeroth moment is an unweighted wall-normal integral and the first moment is a wall-normal integral linearly weighted by wall-normal distance to favor events occurring further from the wall. In addition to wall-normal integration, the fields are also low-pass filtered in the wall-parallel directions,  $\tilde{\phi}$ , where the filter width corresponds to the 2D grid spacing to be used for TRIS.

The filtered zeroth and first moments of (2.1) are

$$\frac{\partial \langle \tilde{u}_i \rangle_0}{\partial x_i} = 0, \quad \frac{\partial \langle \tilde{u}_i \rangle_1}{\partial x_i} = 2 \langle \tilde{v} \rangle_0, \quad (2.5)$$

where the zeroth moment of the wall-parallel velocity,  $\langle \tilde{u}_i \rangle_0$ , is a two-dimensional, two-component (2D/2C) vector field with zero divergence. The first moment of the wall-parallel velocity,  $\langle \tilde{u}_i \rangle_1$ , is also 2D/2C and has divergence equal to (twice) the zeroth moment of the wall-normal velocity,  $\langle \tilde{v} \rangle_0$ . In this way, the inclusion of the first moment provides a three-component (2D/3C) description of the zeroth-moment velocity field.

The first moment of mass conservation, (2.5), compactly describes the relationship between streamwise rolls and sweeps/ejections (characterized by  $\partial \langle \tilde{u}_2 \rangle_1 / \partial x_2$  and  $\langle \tilde{v} \rangle_0$ , respectively) that are responsible for the formation of streamwise-oriented streaks. This relationship is illustrated in figure 1, which views a streamwise roll-streak flow pattern in the spanwise-normal plane. In this view, a clockwise roll corresponds to a positive first-moment of spanwise velocity,  $\langle \tilde{u}_2 \rangle_1 > 0$ , and a counter-clockwise roll corresponds to  $\langle \tilde{u}_2 \rangle_1 < 0$ . The negative or positive gradients in between two counter-rotating rolls correspond to negative or positive wall-normal velocities, in accordance with (2.5). These sweeps and ejections, respectively, transport fluid across the mean velocity gradient leading to high and low speed streaks in between the rolls. The interplay between streamwise rolls and streaks is crucial for the self-sustaining process of near-wall streaks (Jiménez & Moin 1991). At high Reynolds number, recent evidence suggests that there exists a similar self-sustaining mechanism for large and very-large scale motions (Cossu & Hwang 2017; Lee & Moser 2019; Zhou *et al.* 2022).

The dynamics of the zeroth and first moment velocity fields are given, respectively, by the zeroth and first moment of (2.2), also including the wall-parallel filtering,

$$\frac{\partial \langle \tilde{u}_i \rangle_0}{\partial t} + \frac{\partial \langle \tilde{u}_i \tilde{u}_j \rangle_0}{\partial x_j} = -\frac{\partial \langle \tilde{p} \rangle_0}{\partial x_i} + \frac{1}{Re_\tau} \frac{\partial^2 \langle \tilde{u}_i \rangle_0}{\partial x_j \partial x_j} - \tilde{\tau}_i + \delta_{i1}, \quad (2.6)$$

$$\frac{\partial \langle \tilde{u}_i \rangle_1}{\partial t} + \frac{\partial \langle \tilde{u}_i \tilde{u}_j \rangle_1}{\partial x_j} = 2 \langle \tilde{u}_i \tilde{v} \rangle_0 - \frac{\partial \langle \tilde{p} \rangle_1}{\partial x_i} + \frac{1}{Re_\tau} \frac{\partial^2 \langle \tilde{u}_i \rangle_1}{\partial x_j \partial x_j} - \frac{2\tilde{u}_{i,\text{top}}}{Re_\tau} + \delta_{i1}, \quad (2.7)$$

where  $\tilde{\tau}_i$  is the instantaneous (dimensionless) wall shear stress (2D/2C) and  $\tilde{u}_{i,\text{top}}$  is the wall-parallel velocity vector (2D/2C) at the top of the open-channel (where a Neumann BC is imposed). Equations (2.6) and (2.7) contain unclosed terms that need to be modeled:  $\tilde{\tau}_i$ ,  $\langle \tilde{u}_i \tilde{u}_j \rangle_0$ ,  $\langle \tilde{u}_i \tilde{u}_j \rangle_1$ ,  $\langle \tilde{u}_i \tilde{v} \rangle_0$ , and  $\tilde{u}_{i,\text{top}}$ . The divergence of (2.6) and (2.7) provide elliptic equations for the pressure moments,  $\langle \tilde{p} \rangle_0$  and  $\langle \tilde{p} \rangle_1$ ,

$$\frac{\partial^2 \langle \tilde{p} \rangle_0}{\partial x_j \partial x_j} = -\frac{\partial^2 \langle \tilde{u}_i \tilde{u}_j \rangle_0}{\partial x_i \partial x_j} - \frac{\partial \tilde{\tau}_j}{\partial x_j}, \quad (2.8)$$

$$\frac{\partial^2 \langle \tilde{p} \rangle_1}{\partial x_j \partial x_j} = 2[\tilde{p}_{\text{top}} - \tilde{p}_{\text{bot}}] - \frac{\partial^2 \langle \tilde{u}_i \tilde{u}_j \rangle_1}{\partial x_i \partial x_j} + 4 \frac{\partial \langle \tilde{u}_i \tilde{v} \rangle_0}{\partial x_i}. \quad (2.9)$$

The zeroth moment of (2.3) has been used to simplify (2.9). Here,  $\tilde{p}_{\text{top}}$  and  $\tilde{p}_{\text{bot}}$  are the pressures at the top and bottom of the open-channel, respectively, and their difference must be modeled to close the system of equations.

### 3. Turbulence Resolution Estimate

Before introducing closure models for (2.6)-(2.9), it is worthwhile to consider how much of the turbulent motions can be captured in this 2D/3C representation of the flow. This is accomplished by asking a more specific question in terms of the turbulent enhancement of the skin friction coefficient,  $C_f = 2\bar{\tau}_1/(\rho\bar{u}_{\text{top}}^2)$ , relative to a laminar flow with the same  $Re_{\text{top}} = \rho\bar{u}_{\text{top}}h/\mu$ . The  $\bar{\phi}$  operator denotes a Reynolds average, and the fluctuation about the mean is  $\phi' = \phi - \bar{\phi}$ . Subtracting (2.7) from (2.6) and averaging,

$$1 = 2 \frac{\bar{u}_{\text{top}}}{Re_\tau} + 2 \langle -\overline{u'v'} \rangle_0 = \frac{\frac{4}{Re_{\text{top}}} + \frac{\langle -4\overline{u'v'} \rangle_0}{\bar{u}_{\text{top}}^2}}{C_f} = \frac{C_{f,\text{lam}} + C_{f,\text{turb}}}{C_f}, \quad (3.1)$$

where  $C_{f,\text{lam}} = 4Re_{\text{top}}^{-1}$  is the skin friction coefficient of a laminar open-channel flow, therefore  $C_{f,\text{turb}} = -4 \langle \overline{u'v'} \rangle_0 / \bar{u}_{\text{top}}^2$  represents the turbulent enhancement of the skin friction coefficient relative to the laminar state. This type of equation was previously introduced as the Angular Momentum Integral (AMI) equation by Elnahas & Johnson (2022) for spatially-developing boundary layers. The turbulent enhancement,  $C_{f,\text{turb}}$ , is partially resolved by the 2D/3C zeroth moment velocity vector field,  $\langle \overline{u'v'} \rangle_0 = \langle \tilde{u} \rangle_0' \langle \tilde{v} \rangle_0' + \langle \overline{u''v''} \rangle_0$ , where  $\phi'' = \phi' - \langle \tilde{\phi} \rangle_0'$  is the unresolved portion of a fluctuating field when integrated in the wall-normal direction and filtered in the wall-parallel directions. Thus, the turbulent skin friction enhancement is the sum of a resolved and unresolved portion,  $C_{f,\text{turb}} = C_{f,\text{res}} + C_{f,\text{unres}}$ . Equation (3.1) is also true for the bottom half of a full-channel flow where  $\bar{u}_{\text{top}}$  corresponds to the average centerline velocity and  $h$  is the half-height of the full-channel.

DNS was used to compute the resolved and unresolved components of the Reynolds shear stress for  $180 \leq Re_\tau \leq 5200$  on a domain size of  $L_x = 8\pi$  and  $L_z = 3\pi$ . The lower

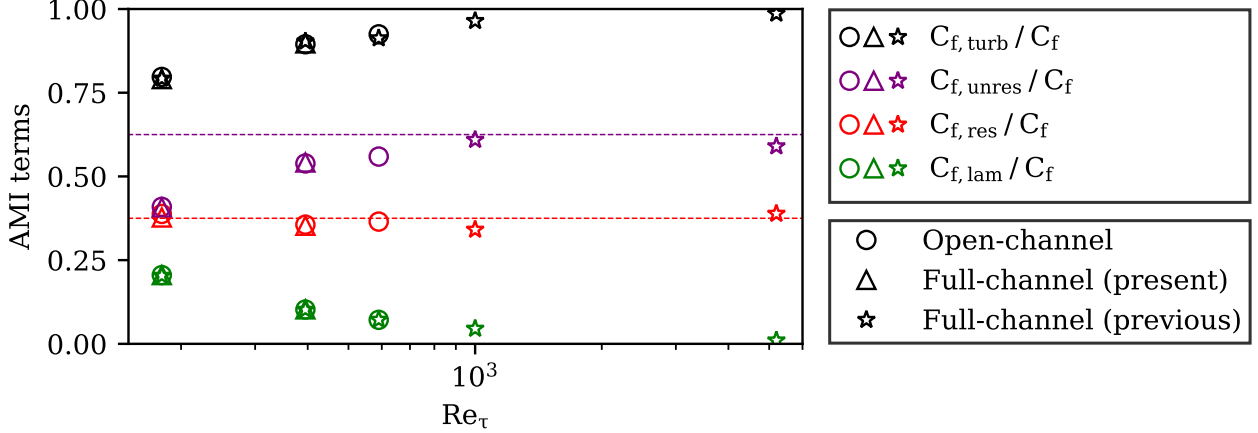


Figure 2: Decomposition of the total skin friction in (3.1). The circular and triangular markers associate with the authors’ open-channel and full-channel flow simulations, respectively. The star marker corresponds to full-channel flow simulations from previous work (Moser *et al.* 1999; Lee & Moser 2015; Graham *et al.* 2016). The colors black, purple, red, and green represents the total, unresolved, and resolved skin friction by turbulent enhancement, and laminar skin friction, respectively. The purple and red dashed lines are at values of  $\frac{5}{8}$  and  $\frac{3}{8}$ , respectively.

friction Reynolds number flows ( $Re_\tau = 180, 395, 590$ ) were simulated using a second-order, staggered finite difference code (Lozano-Durán *et al.* 2018) for both full-channel and open-channel configurations and the data for the larger Reynolds numbers ( $Re_\tau = 1000, 5200$ ) are from the Johns Hopkins Turbulence Databases (Graham *et al.* 2016; Lee & Moser 2015). The results using a spectral cutoff filter with  $k_{cut}h = 16$  (applied to the streamwise and spanwise directions) are shown in figure 2. The estimated statistical convergence error, following Shirian *et al.* (2023), is approximately the size of the symbols used (or smaller), and is further discussed in the Supplementary Material. There is no noticeable difference between open-channel and full-channel flow results for the smaller Reynolds number simulations, justifying the use of existing full-channel flow datasets (at higher Reynolds number) to make rough estimates for the open-channel configuration. As expected, the laminar skin friction decays with increasing  $Re_\tau$ , so the sum of the resolved and unresolved turbulent enhancement approaches unity. The unresolved portion generally increases with  $Re_\tau$  and appears to approach an asymptotic value based on the available data. Assuming the observed trends continue, it may be estimated that the TRIS equations derived in §2 can resolve approximately 35–40% of the turbulent skin friction enhancement at large Reynolds numbers using a numerical resolution of  $\sim h/5$  in the wall-parallel directions. Finer wall-parallel resolution does not significantly increase  $C_{f,res}$  (Ragan *et al.* 2025).

#### 4. Closure Approximations

To perform a TRIS calculation, a few unclosed terms in (2.6)-(2.9) need to be approximated in terms of the resolved 2D fields. The present objective is to demonstrate the sufficiency of the framework presented in §2 for supporting self-sustaining turbulent fluctuations with realistic structure. To this end, a simple closure is presented by writing the wall-parallel velocity as  $\tilde{u}_i = U_i + U_i''$ , where  $U_i(x_1, x_2, y, t)$  is interpreted as the mean velocity profile conditioned on the local resolved state defined by  $\langle \tilde{u}_i \rangle_0(x_1, x_2, t)$  and  $\langle \tilde{u}_i \rangle_1(x_1, x_2, t)$ . For

now, this conditional mean profile is modeled using a skewed Coles profile (Coles 1956),

$$U_i = \left[ \frac{1}{\kappa} \ln y + \left( \frac{1}{\kappa} \ln Re_* + B \right) \right] e_{i,*} + \left[ \frac{2\Pi}{\kappa} \sin^2 \left( \frac{\pi}{2} y \right) \right] e_{i,\Pi}, \quad (4.1)$$

where  $\kappa = 0.41$  is the inverse log slope and  $B$  is the log vertical intercept, parameters that are pre-set. The local friction Reynolds number is  $Re_*(x_1, x_2, t)$  and  $\Pi(x_1, x_2, t)$  is the local wake parameter. The 2D unit vectors  $e_{i,*}(x_1, x_2, t)$  and  $e_{i,\Pi}(x_1, x_2, t)$  align with the  $Re_*$  and  $\Pi$ , respectively. The local values of  $Re_*$ ,  $\Pi$ ,  $e_{i,*}$ , and  $e_{i,\Pi}$  are uniquely determined at each point in the  $x_1 - x_2$  plane given the local resolved state defined by the zeroth and first moments,  $\langle \widetilde{u}_i \rangle_0 = \langle U_i \rangle_0$  and  $\langle \widetilde{u}_i \rangle_1 = \langle U_i \rangle_1$ , where it is assumed that the integral moments of the fluctuations about the conditionally averaged velocity profiles are neglected.

Equation (4.1) is evaluated at  $y = 1$  to close  $\widetilde{u}_{i,\text{top}}$ . The local wall shear stress  $\widetilde{\tau}_i$  is tied to the log portion of the assumed profile in (4.1),

$$\widetilde{\tau}_i = \left( \frac{Re_*}{Re_\tau} \right)^2 e_{i,*}. \quad (4.2)$$

The zeroth and first moments of  $\widetilde{u}_i \widetilde{u}_j$  are closed by decomposing the term into a portion that is resolved by the Coles profile and unresolved ( $\sigma_{0,ij}$  and  $\sigma_{1,ij}$ ),

$$\langle \widetilde{u}_i \widetilde{u}_j \rangle_0 = \langle U_i U_j \rangle_0 + \sigma_{0,ij}, \quad \langle \widetilde{u}_i \widetilde{u}_j \rangle_1 = \langle U_i U_j \rangle_1 + \sigma_{1,ij}. \quad (4.3)$$

The resolved portion can be directly computed from the assumed profile, while the unresolved part is modeled by a wall-parallel eddy viscosity approximation,  $\sigma_{0,ij} = C_s \Delta^2 \sqrt{\langle S_{mn} \rangle_0} \langle S_{mn} \rangle_0 \langle S_{ij} \rangle_0$  and  $\sigma_{1,ij} = C_s \Delta^2 \sqrt{\langle S_{mn} \rangle_1} \langle S_{mn} \rangle_1 \langle S_{ij} \rangle_1$ , where  $C_s = 0.78$  is chosen to be a small value that is still large enough to ensure stability,  $S_{ij}$  is the wall-parallel strain rate tensor, and  $\Delta$  is the grid spacing (filter width). The resolved portions,  $\langle U_i U_j \rangle_0$  and  $\langle U_i U_j \rangle_1$ , are linearized about reference (mean) values for the log offset,  $B$ , and the Coles wake strength,  $\Pi_{\text{ref}}$ , which are set to match the mean zeroth and first moment of the streamwise velocity computed from DNS.

The  $\langle \widetilde{u}_i \widetilde{v} \rangle_0$  term is also decomposed into a resolved and unresolved component,

$$\langle \widetilde{u}_i \widetilde{v} \rangle_0 = \langle U_i \rangle_0 \langle \widetilde{v} \rangle_0 + \langle u_i'' v'' \rangle_0. \quad (4.4)$$

Here,  $\langle u_i'' v'' \rangle_0$  is modeled using an eddy viscosity with an attached eddy scaling,

$$-2 \langle u_i'' v'' \rangle_0 = C_{uv} \frac{[1 + (1 - C_\Pi) \Pi_{\text{ref}}] e_{i,*} + C_\Pi \Pi e_{i,\Pi}}{1 + \Pi_{\text{ref}}}, \quad (4.5)$$

where  $C_{uv}$  is set using the AMI balance (the purple symbols in figure 2) and  $C_\Pi$  is tuned to allow for the correct amount of resolved Reynolds shear stress,  $\langle U_i \rangle_0 \langle \widetilde{v} \rangle_0$  (the red symbols in figure 2). Lastly, the pressure difference between the top and bottom of the open-channel is closed by assuming a linear pressure profile at each location,  $\widetilde{p}_{\text{top}} - \widetilde{p}_{\text{bot}} = 6 [\langle \widetilde{p} \rangle_1 - \langle \widetilde{p} \rangle_0]$ . A detailed derivation of the closure approximation along with the numerical values of the model coefficients are available in the Supplementary Material.

## 5. Results and Discussion

A Python code was developed to solve (2.6)-(2.9) together with the closure models described in §4 using a pseudo-spectral approach on a doubly-periodic domain of size  $L_x = 8\pi$  and  $L_z = 3\pi$  to match the DNS domain. The maximum dimensionless wavenumber is  $k_{\text{max}} h = k_{\text{cut}} h = 16$  in the wall-parallel directions, such that the grid spacing based on collocation points is  $\Delta = \pi/16 \approx \frac{1}{5}$  (five grid points per half-channel thickness). Initially



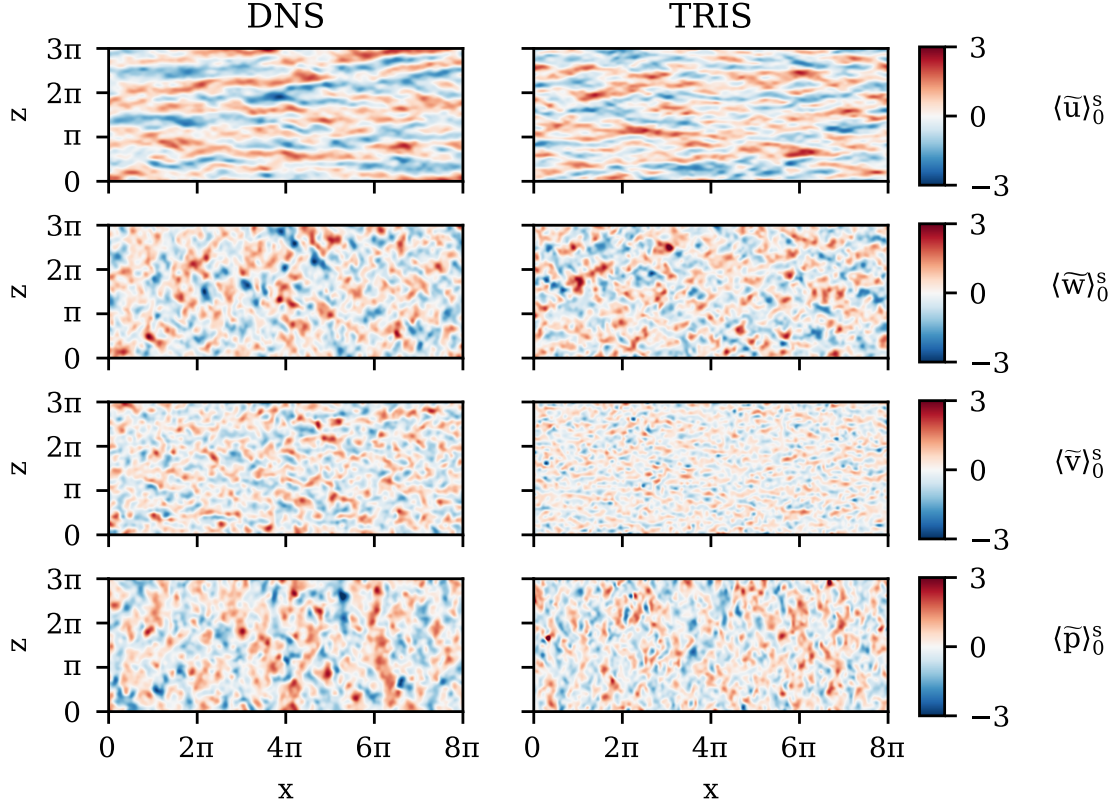


Figure 3: Instantaneous snapshots of the standardized (denoted by a superscript  $s$ )  $\langle \tilde{u} \rangle_0$ ,  $\langle \tilde{w} \rangle_0$ ,  $\langle \tilde{v} \rangle_0$ , and  $\langle \tilde{p} \rangle_0$  fields in descending order at  $Re_\tau = 395$ . Snapshots are based on the field imposed by a spectral cutoff filter of  $k_{\text{cut}}h = 16$  for DNS (left column) to match the grid resolution of TRIS (right column). Videos of the temporal evolution of these fields are available in Supplementary Material. For TRIS specifically, a Python code running the time progression of this snapshot through Jupyter notebook is available at [https://cocalc.com/share/public\\_paths/fa88e6bf9eea2307452e4f69f0a3bf7f8c65d8bd/figure-3](https://cocalc.com/share/public_paths/fa88e6bf9eea2307452e4f69f0a3bf7f8c65d8bd/figure-3).

( $t = 0$ ),  $\langle \tilde{u} \rangle_0$  is set to a uniform field based on the approximate mean velocity,  $\langle \tilde{u} \rangle_1$  and  $\langle \tilde{w} \rangle_0$  are initialized to zero, while  $\langle \tilde{w} \rangle_1$  is initialized with white noise.

The TRIS simulation at  $Re_\tau = 395$  reaches a statistically stationary state with streamwise-oriented streaky structures that exhibit self-sustaining dynamics, as shown in the top row of figure 3. The TRIS results on the right-side column are in comparison with (filtered) zeroth moment fields from DNS on the left-side column. In order to emphasize flow structure, all fields in figure 3 are standardized (denoted with a superscript  $s$ ), i.e., fluctuations normalized by their standard deviation. While  $\langle \tilde{u} \rangle_0^s$  (top row) exhibit relatively realistic streaky structure,  $\langle \tilde{w} \rangle_0^s$  and  $\langle \tilde{v} \rangle_0^s$  (second and third row, respectively) do not show similar streaks in the TRIS results, in agreement with the flow structure observed from the DNS results. Similarly,  $\langle \tilde{p} \rangle_0^s$  (last row) do not contain streamwise-oriented streaks. These TRIS results demonstrate that the 2D-based integral moment equations, derived from the Navier-Stokes equations, are sufficient to generate self-sustaining turbulence with qualitatively realistic structure in a 2D/3C representation.

Given the DNS results in §3, TRIS is also evaluated in terms of the fraction of turbulence it resolves. For the results shown in this paper, closure parameters have been set or tuned (see Supplementary Material) in order to match within 1% of the mean  $\langle \tilde{u} \rangle_0$  and  $\langle \tilde{u} \rangle_1$ , as well as the AMI balance, formulated in (3.1) and plotted in figure 2. Therefore, the TRIS formulation shown here is not (yet) predictive in an engineering sense, which would require

the development of physics-based closures beyond the scope of this work. Importantly, it is demonstrated here that the theoretical resolution of 35 – 40% of the Reynolds shear stress can be achieved with the present formulation, however simple it may be. With little-to-no effort to optimize the computational runtime, a flow through time for a domain of length  $L_x = 8\pi$  takes  $\sim 1$  minute on a single processor with a desktop computer. Furthermore, simulations up to  $Re_\tau = 10^6$  were performed without increase in computational cost. More details of TRIS results for a range of Reynolds numbers are shown in the Supplemental Material.

For an evaluation of the present TRIS formulation in terms of quantities that are not set or tuned via closure parameter manipulation, the streamwise and spanwise (co-)spectra of the Reynolds shear stress and three kinetic energy components are shown in figure 4 for  $Re_\tau = 395$  and  $Re_\tau = 590$ . Here,  $k_i$  is nondimensionalized by the height of the open-channel,  $h$ . The top row shows the co-spectra for the Reynolds shear stress. The sum of the co-spectra over all streamwise ( $k_1 = k_x$ ) or spanwise ( $k_2 = k_z$ ) modes is the zeroth-moment of the Reynolds shear stress as it shows up in the AMI balance, (3.1), which matches the DNS by means of parameter tuning. More interestingly, the TRIS results show a good degree of success in replicating the shape of the distribution of the Reynolds shear stress as a function of both streamwise (red) and spanwise (blue) wavenumber. In keeping with the structure observed in figure 3, the co-spectrum peaks at the lowest streamwise wavenumber and at an intermediate spanwise wavenumber. The TRIS results thus reproduce this basic structure, although the spectrum peaks at a larger spanwise wavenumber compared to DNS, which is related to the observation from figure 3 that the typical streak width is generally under-predicted by the current TRIS formulation.

The final three rows of figure 4 show the spectra for each of the three components of kinetic energy: streamwise, spanwise, and wall-normal, respectively. The shape of the streamwise and spanwise spectra produced by the present TRIS formulation are generally similar to the DNS results, but with lower overall magnitude. That is, the root-mean-square of  $\langle \tilde{u} \rangle_0$  and  $\langle \tilde{w} \rangle_0$  are under-predicted by TRIS. On the other hand, the  $\langle \tilde{v} \rangle_0$  root-mean-square shows an over-prediction by TRIS. Statistics of TRIS and DNS are tabulated in the Supplementary Material. For the wall-normal velocity component, the shape of the TRIS spectra with respect to  $k_1$  is relatively accurate. TRIS shows a peak at the highest resolved  $k_2$ , however, which is qualitatively different than the DNS spectrum. The authors speculate that a more accurate pressure model, for  $\tilde{p}_{\text{top}} - \tilde{p}_{\text{bot}}$ , could help TRIS produce a more accurate spectra of wall-normal fluctuations with respect to spanwise wavenumber. This could in turn also help yield a more accurate distribution of kinetic energy between the three components. Further work developing physics-based models is deferred to future work. Note that the current results reflect TRIS simulations with model coefficients tuned for the specific domain size and grid spacing employed, and these coefficients require retuning for different choices of grid spacing and domain size.

This paper introduces a framework for Turbulence-Resolving Integral Simulations (TRIS) of wall-bounded flows. A proof-of-concept demonstration is shown for an open-channel configuration using instantaneous moment-of-momentum integral equations (derived from first principles) with closures based on an assumed profile. The use of zeroth- and first-moment integral equations in a 2D (streamwise-spanwise) domain provides a sufficient basis for reproducing the self-sustaining process of large-scale streaks in wall-bounded turbulence. The resulting 2D/3C TRIS simulations yield a qualitatively realistic structure for the three velocity components and pressure fields, and quantitative differences with DNS are documented. With wall-parallel resolution of  $h/5$ , DNS evidence suggests that the approach can directly resolve 35 – 40% of the Reynolds shear stress responsible for turbulent skin friction enhancement, at arbitrarily large Reynolds number, according to the AMI equation. The cost of TRIS is very low compared to established turbulence-resolving techniques such



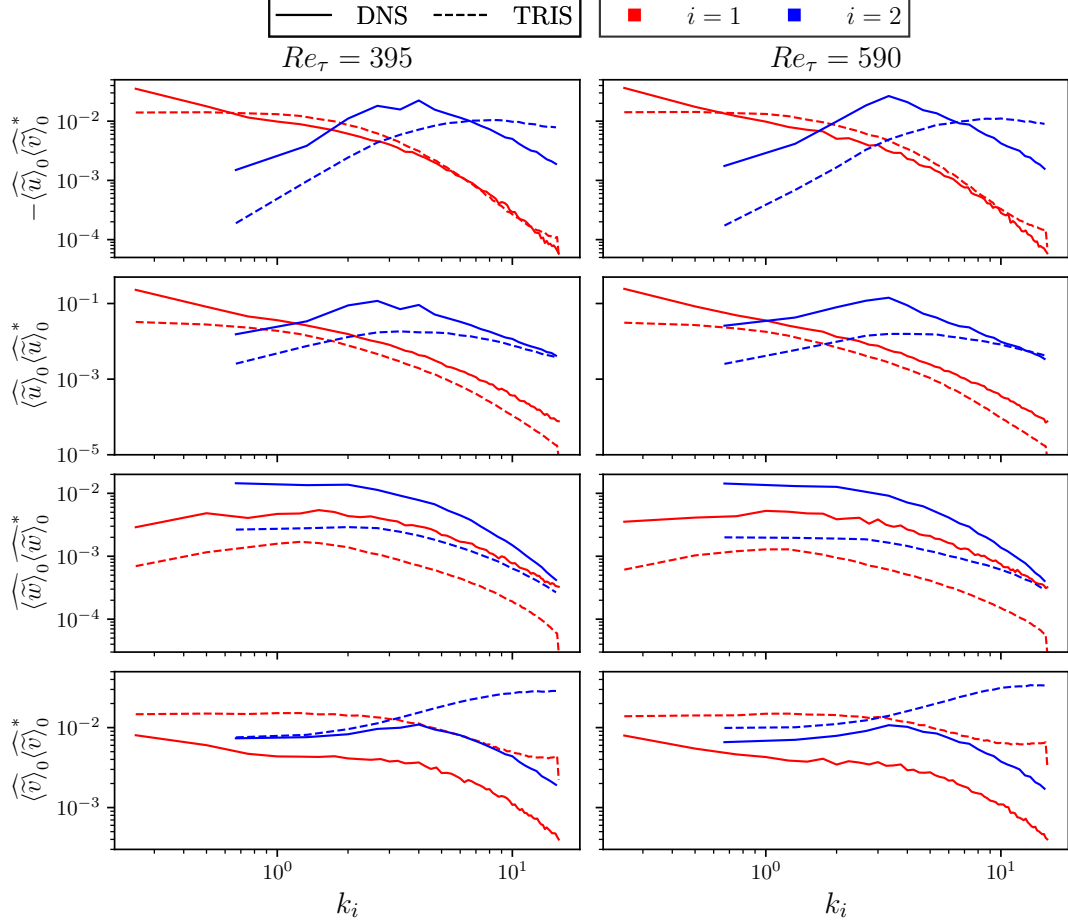


Figure 4: Streamwise (red) and spanwise (blue) spectral distributions of the resolved shear, streamwise, spanwise, and wall-normal Reynolds stress components in descending order at  $Re_\tau = 395$  (left) and  $Re_\tau = 590$  (right). The Fourier transform,  $\hat{\phi}$  of the resolved velocity is multiplied by its complex conjugate,  $\hat{\phi}^*$ . The solid and dashed lines represent DNS and TRIS, respectively, and  $k_i$  is non-dimensionalized by the height of the open-channel,  $h$ .

as LES and DNS, with one flow-through time taking  $\sim 1$  minute on a single processor for a channel flow with arbitrarily high Reynolds number using an unoptimized Python code.

A related quasi-2D/3C approach to reduced-order modeling of self-sustaining wall-bounded turbulence is the restricted nonlinear (RNL) model (Thomas *et al.* 2014), which resolves the flow in the spanwise and wall-normal directions while severely restricting the representation of streamwise variations. In comparison, the TRIS approach is well suited for extension to a more general class of flows that are not periodic in the streamwise (or spanwise) direction. Ongoing and future work aims to formulate the TRIS equations for boundary layer flows, including interactions with an irrotational freestream flow with pressure gradients. The ability of TRIS to resolve large-scale motions, which have important sensitivities to favorable and adverse pressure gradients, motivates future development targeting engineering-relevant flows. Importantly, a truly predictive approach (for engineering quantities of interest) requires more work to establish physics-based closure models to improve the accuracy and general applicability of TRIS compared to the present proof of concept.

## Acknowledgements

TR was supported by the Department of Defense (DoD) National Defense Science & Engineering Graduate (NDSEG) Fellowship Program. MW and SS were supported by the Air Force Office of Scientific Research under award number FA9550-24-1-0127. PJ was supported by the National Science Foundation under CAREER award No. 2340121.

## Declaration of Interests.

The authors report no conflict of interest.

## REFERENCES

- COLES, DONALD 1956 The law of the wake in the turbulent boundary layer. *J. Fluid Mech.* **1** (2), 191–226.
- COSSU, C. & HWANG, Y. 2017 Self-sustaining processes at all scales in wall-bounded turbulent shear flows. *Philos. Trans. R. Soc. A* **375** (2089), 20160088.
- DRELA, M. 1989 XFOIL: an analysis and design system for low reynolds number airfoils. In *Low Reynolds Number Aerodynamics: Proceedings of the Conference Notre Dame, Indiana, USA, 5–7 June 1989*, pp. 1–12. Springer.
- ELNAHHAS, AHMED & JOHNSON, PERRY L. 2022 On the enhancement of boundary layer skin friction by turbulence: an angular momentum approach. *J. Fluid Mech.* **940**, A36.
- GOC, K., BOSE, S. & MOIN, P. 2020 Wall-modeled large eddy simulation of an aircraft in landing configuration. In *AIAA Aviation 2020 Forum*, p. 3002.
- GRAHAM, J., KANOV, K., YANG, X. I. A., LEE, M., MALAYA, N., LALESCU, C. C., BURNS, R., EYINK, G., SZALAY, A., MOSER, R. D. & MENEVEAU, C. 2016 A web services accessible database of turbulent channel flow and its use for testing a new integral wall model for les. *JoT* **17** (2), 181–215.
- GUALA, M., HOMMEMA, S. E. & ADRIAN, R. J. 2006 Large-scale and very-large-scale motions in turbulent pipe flow. *J. Fluid Mech.* **554**, 521–542.
- JIMÉNEZ, J. & MOIN, P. 1991 The minimal flow unit in near-wall turbulence. *J. Fluid Mech.* **225**, 213–240.
- KLINE, S. J., MORKOVIN, M. V., SOVRAN, G. & COCKRELL, D. J., ed. 1968 *Computation of Turbulent Boundary Layers – 1968 AFOSR-IFP Stanford Conference*, , vol. 1, Stanford University.
- LEE, M. & MOSER, R. D. 2015 Direct numerical simulation of turbulent channel flow up to  $Re_\tau = 5200$ . *J. Fluid Mech.* **774**, 395–415.
- LEE, MYOUNGKYU & MOSER, ROBERT D. 2019 Spectral analysis of the budget equation in turbulent channel flows at high reynolds number. *J. Fluid Mech.* **860**, 886–938.
- LOZANO-DURÁN, A., HACK, M. J. P. & MOIN, P. 2018 Modeling boundary-layer transition in direct and large-eddy simulations using parabolized stability equations. *Phys. Rev. Fluids* **3**, 023901.
- MOSER, R. D., KIM, J. & MANSOUR, N. N 1999 Direct numerical simulation of turbulent channel flow up to  $Re_\tau = 590$ . *Phys. Fluids* **11** (4), 943–945.
- RAGAN, T., WARNECKE, M. & JOHNSON, P. L. 2025 The effect of spatial filtering on instantaneous wall-normal integrals. *AIAA SciTech Forum AIAA 2025-2219*.
- SHIRIAN, YASAMAN, HORWITZ, JEREMY A.K. & MANI, ALI 2023 On the convergence of statistics in simulations of stationary incompressible turbulent flows. *Comput. Fluids* **266**, 106046.
- SPALART, P. R. 2000 Strategies for turbulence modelling and simulations. *Int. J. Heat Fluid Flow* **21** (3), 252–263.
- THOMAS, V. L., LIEU, B. K., JOVANOVIĆ, M. R., FARRELL, B. F., IOANNOU, P. J. & GAYME, D. F. 2014 Self-sustaining turbulence in a restricted nonlinear model of plane Couette flow. *Phys. Fluids* **26** (10), 105112.
- UNGARISH, M. 2010 *An Introduction to Gravity Currents and Intrusions*. CRC Press.
- YANG, X. I. A. & GRIFFIN, K. P. 2021 Grid-point and time-step requirements for direct numerical simulation and large-eddy simulation. *Phys. Fluids* **33** (1), 015108.
- ZHOU, ZISONG, XU, CHUN-XIAO & JIMÉNEZ, JAVIER 2022 Interaction between near-wall streaks and large-scale motions in turbulent channel flows. *J. Fluid Mech.* **940**, A23.

Banner appropriate to article type will appear here in typeset article

arXiv:2501.02121v1 [physics.flu-dyn] 3 Jan 2025

# Turbulence-Resolving Integral Simulations for Wall-Bounded Flows

Tanner Ragan<sup>1†</sup>, Mark Warnecke<sup>1‡</sup>, Samuel Stout<sup>1¶</sup> and Perry L. Johnson<sup>1||</sup>

<sup>1</sup>University of California Irvine, Mechanical and Aerospace Engineering Department, Samueli School of Engineering, Irvine, CA, USA

(Received xx; revised xx; accepted xx)

## Supplementary Material

### A. Statistical Convergence

For the lower friction Reynolds number flows ( $Re_\tau = 180, 395, 590$ ), the Navier-Stokes equations are solved on a staggered Cartesian grid using a second-order central difference scheme in the wall-parallel directions and an explicit third-order Runge-Kutta scheme for time advancement (Lozano-Durán *et al.* 2018). Full-channel flow simulations were executed and compared against Moser *et al.* (1999) to ensure proper spatial discretization for the open-channel flow application. These lower Reynolds number simulations were ran out for twenty large-eddy turnover times. For the higher friction Reynolds number flows ( $Re_\tau = 1000, 5200$ ), velocity data was gathered from John Hopkins Turbulence Database (Graham *et al.* 2016; Lee & Moser 2015), where the solver uses a Fourier-Galerkin pseudo-spectral method for the wall-parallel directions and a third-order Runge-Kutta scheme for time advancement. These simulations were ran out for roughly one large-eddy turnover time.

To ensure the viability of DNS executed by the authors, statistical quantities of the mean velocity and root-mean-square profiles are compared against Moser *et al.* (1999). The top row of figure [S1](#) illustrates that the current DNS simulations (at  $Re_\tau = 180, 395$ ) accurately captures mean velocity profiles for the full-channel flow. Here, the grey dashed lines correspond to the fits of the viscous sub-layer and log-layer region. The top row of figure [S2](#) further shows that, in the full-channel configuration, the root-mean-square statistics sufficiently matches with Moser *et al.* (1999). This analysis demonstrates sufficient spatial discretization, providing confidence in the accuracy of DNS on the open-channel configuration for  $180 \leq Re_\tau \leq 590$ .

Further comparison of the full-channel and open-channel configurations are illustrated in the bottom rows of figure [S1](#) and [S2](#). Here, the profile in the full-channel flow extends from the bottom wall (no-slip) to the centerline (no boundary condition) whereas the profile in the open-channel flow extends from the bottom wall (no-slip) to the top boundary (no-vorticity). Interestingly, the mean velocity profiles are statistically identical between these two

† Email address for correspondence: ragant@uci.edu

‡ Email address for correspondence: mwarneck@uci.edu

¶ Email address for correspondence: stoutst@uci.edu

|| Email address for correspondence: perry.johnson@uci.edu

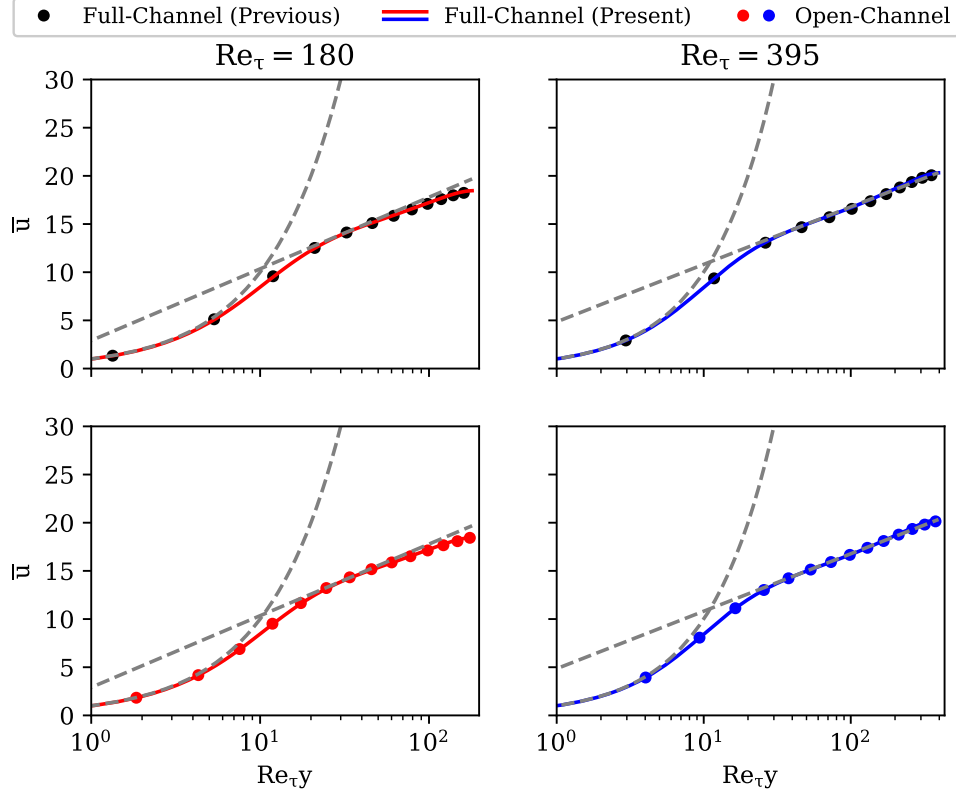


Figure S1: Reynolds averaged mean velocity profiles of channel flows at  $Re_\tau = 180$  (left column) and  $Re_\tau = 395$  (right column). The “Full-Channel (Previous)” label (black circular markers) corresponds to the profiles gathered from Moser *et al.* (1999) whereas the “Full-Channel (Present)” and “Open-Channel” labels (colored lines and circular markers, respectively) correspond to the author’s DNS data.

configurations. However, notable discrepancies are observed in the root-mean-square velocity profiles for  $Re_\tau y \gtrsim 125$ , caused by the no-penetration condition at the top boundary. This boundary condition enforces the wall-normal fluctuations to be zero, causing the streamwise and spanwise fluctuations to increase at the top wall.

The statistical convergence of the resolved skin friction,  $C_{f,\text{res}}$ , in (3.1) is further analyzed. Since large-scale motions (contributing to  $C_{f,\text{res}}$ ) tend to have longer turnover times than smaller scales (contributing to  $C_{f,\text{unres}}$ ),  $C_{f,\text{unres}}$  is more statistically converged than its resolved counterpart. As used by Shirian *et al.* (2023), the estimated statistical convergence error (or standard error of the mean) is computed with

$$\phi_{\text{error}} = \frac{1}{N} \sqrt{\sum_{i=1}^N (\phi_{i,w} - \phi_m)^2}, \quad (\text{S1})$$

where  $N$  is the number of time windows,  $\phi_{i,w}$  is the average quantity across a particular time window, and  $\phi_m$  is the statistically converged average quantity (Ross 1998). According to Shirian *et al.* (2023), estimates of the statistical error can reasonably be computed across  $N = 4$  windows with a window length of 10 turnover times on a full-channel flow with a domain size of  $L_x = 2\pi$  and  $L_z = 1\pi$ . With the present DNS simulations running on a domain size of  $L_x = 8\pi$  and  $L_z = 3\pi$ , which is 12 times larger than the previously mentioned domain size, the number of windows and window lengths are modified.

For the lower Reynolds number channel flow simulations ( $Re_\tau = 180, 395, 590$ ), (S1) of

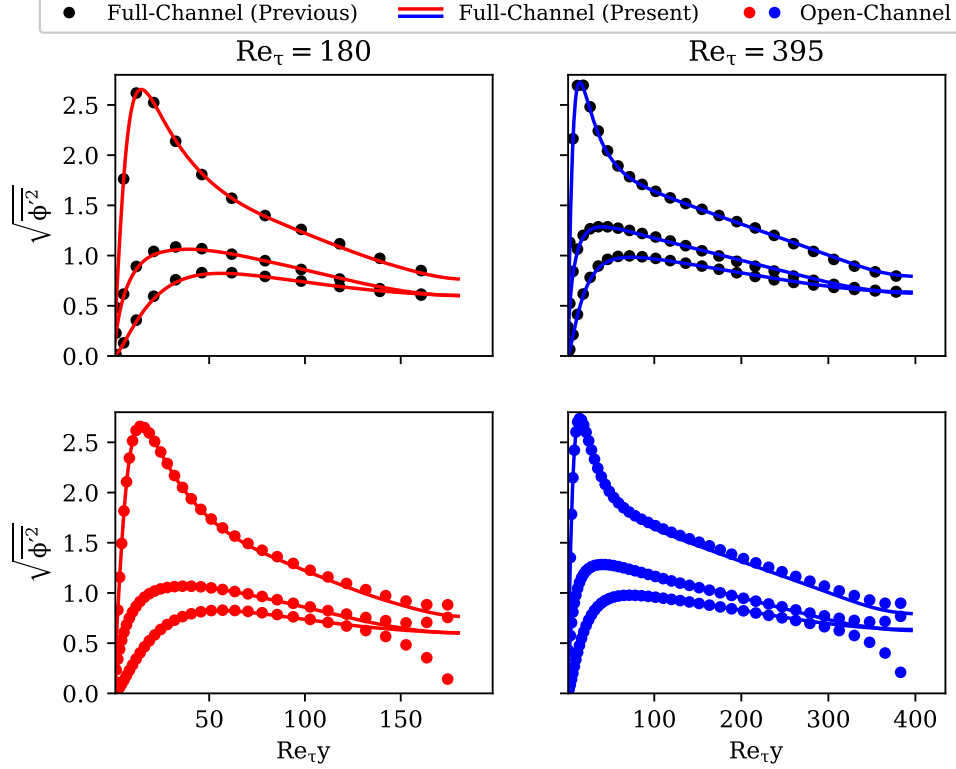


Figure S2: Root-mean-square profiles of channel flows at  $Re_\tau = 180, 395$  (left and right columns, respectively). “Full-Channel (Previous)”, denoted by the black circular markers, corresponds to the profiles gathered from Moser *et al.* (1999) while “Full-Channel (Present)” and “Open-Channel” (denoted by colored lines and circular markers, respectively) correspond to the author’s DNS data. In all sub-plots, the streamwise, spanwise, and wall-normal components are distributed in descending order.

$C_{f,res}$  is computed across  $N = 20$  windows with window lengths of 1 turnover time. The estimated statistical error of  $C_{f,res}$  is less than 1.0%. Alternatively, for the higher Reynolds number simulations ( $Re_\tau = 1000, 5200$ ), the error of  $C_{f,res}$  is computed across  $N = 2$  windows with window lengths of about 1 turnover time. It turns out that the maximum  $\phi_{error}$  value of  $C_{f,res}$  is approximately 2.0%.

Higher confidence of the estimated error of the averaged  $C_{f,res}$  is placed in the lower  $Re_\tau$  values since more windows are available to compute over. The corresponding estimated values for higher  $Re_\tau$  are (very) rough approximations since more velocity data is required to accurately compute the absolute average ( $\phi_m$ ) of the resolved skin friction by turbulent enhancement (i.e., more time windows are required).

## B. Detailed Derivation of the Models for the Unclosed Terms

For demonstrative purposes, a simple closure is presented by assuming that the skewed Coles wake velocity profile, (4.1), captures the conditionally averaged wall-parallel profiles ( $U_i(x_1, x_2, y, t) = \langle \tilde{u}_i | \langle \tilde{u}_i \rangle_0, \langle \tilde{u}_i \rangle_1 \rangle$ ). To capture the integral moments, (2.4) is applied on  $U_i$ , with the assumption that the moment integrals of the profile fluctuations about the conditional average ( $\langle U_i'' \rangle_0$  and  $\langle U_i'' \rangle_1$ ) are negligible,

$$\langle \tilde{u}_i \rangle_0 = \langle U_i \rangle_0 + \cancel{\langle U_i'' \rangle_0} \approx 0, \quad \langle \tilde{u}_i \rangle_1 = \langle U_i \rangle_1 + \cancel{\langle U_i'' \rangle_1} \approx 0. \quad (S1)$$



Applying (2.4) on (4.1) generates the following relations,

$$\langle U_i \rangle_0 = \left[ \frac{1}{\kappa} (\ln Re_* - 1) + B \right] e_{i,*} + \frac{\Pi}{\kappa} e_{i,\Pi}, \quad (S2)$$

$$\langle U_i \rangle_1 = \left[ \frac{1}{\kappa} \left( \ln Re_* - \frac{1}{2} \right) + B \right] e_{i,*} + \frac{\Pi}{\kappa} \left( 1 + \frac{4}{\pi^2} \right) e_{i,\Pi}, \quad (S3)$$

which are used to solve for  $\ln Re_*$ ,  $e_{i,*}$ ,  $\Pi$ , and  $e_{i,\Pi}$ . Note that  $\kappa = 0.41$  is set for all TRIS simulations. The expressions for these terms are the following,

$$\ln Re_* = \kappa \left| \left( \frac{\pi^2}{4} + 1 \right) \langle \widetilde{u}_i \rangle_0 - \frac{\pi^2}{4} \langle \widetilde{u}_i \rangle_1 \right| - \kappa B + \frac{\pi^2}{8} + 1, \quad (S4)$$

$$e_{i,*} = \frac{\left( \frac{\pi^2}{4} + 1 \right) \langle \widetilde{u}_i \rangle_0 - \frac{\pi^2}{4} \langle \widetilde{u}_i \rangle_1}{\left| \left( \frac{\pi^2}{4} + 1 \right) \langle \widetilde{u}_i \rangle_0 - \frac{\pi^2}{4} \langle \widetilde{u}_i \rangle_1 \right|}, \quad (S5)$$

$$\Pi = \left| \frac{\pi^2}{4} \kappa (\langle \widetilde{u}_i \rangle_1 - \langle \widetilde{u}_i \rangle_0) - \frac{\pi^2}{8} e_{i,*} \right|, \quad (S6)$$

$$e_{i,\Pi} = \frac{1}{\Pi} \left( \frac{\pi^2}{4} \kappa (\langle \widetilde{u}_i \rangle_1 - \langle \widetilde{u}_i \rangle_0) - \frac{\pi^2}{8} e_{i,*} \right). \quad (S7)$$

With this formulations, the local values of the shear stress and top velocity are

$$\widetilde{\tau}_i = \left( \frac{Re_*}{Re_\tau} \right)^2 e_{i,*}, \quad (S8)$$

$$U_{T,i} = \left[ \frac{1}{\kappa} \ln Re_* + B \right] e_{i,*} + \frac{2\Pi}{\kappa} e_{i,\Pi}, \quad (S9)$$

respectively. The pressure is closed by assuming a linear pressure profile that leads to the following relationship between the pressure boundary difference and pressure integral moment difference,

$$\widetilde{p}_{\text{top}} - \widetilde{p}_{\text{bot}} = 6 [\langle \widetilde{p} \rangle_1 - \langle \widetilde{p} \rangle_0]. \quad (S10)$$

For simplicity, the wall-parallel nonlinear terms,  $\langle \widetilde{u}_i \widetilde{u}_j \rangle_0$  and  $\langle \widetilde{u}_i \widetilde{u}_j \rangle_1$ , are split into the resolved and unresolved components captured by the Coles profile,

$$\langle \widetilde{u}_i \widetilde{u}_j \rangle_0 = \langle U_i U_j \rangle_0 + \sigma_{0,ij}, \quad \langle \widetilde{u}_i \widetilde{u}_j \rangle_1 = \langle U_i U_j \rangle_1 + \sigma_{1,ij}, \quad (S11)$$

where  $\sigma_{0,ij}$  and  $\sigma_{1,ij}$  are defined as,

$$\sigma_{0,ij} = C_s \Delta^2 \sqrt{\langle S_{mn} \rangle_0 \langle S_{mn} \rangle_0} \langle S_{ij} \rangle_0, \quad \sigma_{1,ij} = C_s \Delta^2 \sqrt{\langle S_{mn} \rangle_1 \langle S_{mn} \rangle_1} \langle S_{ij} \rangle_1. \quad (S12)$$

Here,  $S_{ij}$  is the strain rate tensor in the wall-parallel directions,  $\Delta$  is the grid spacing of the TRIS simulation, and  $C_s = 0.78$  is the set parameter for the eddy viscosity coefficient. The conditional (resolved) components are quasi-linearized for robustness, defined as,

$$\langle U_i U_j \rangle_0 = A_0(e_{i,*} e_{j,*}) + B_0(e_{i,*} e_{j,*} + e_{i,\Pi} e_{j,\Pi}) + D_0(e_{i,\Pi} e_{j,\Pi}), \quad (S13)$$

$$\langle U_i U_j \rangle_1 = A_1(e_{i,*} e_{j,*}) + B_1(e_{i,*} e_{j,*} + e_{i,\Pi} e_{j,\Pi}) + D_1(e_{i,\Pi} e_{j,\Pi}), \quad (S14)$$

where

$$A_0 = \left(2T_{\text{ref}} - \frac{2}{\kappa}\right)T + \left(\frac{2}{\kappa^2} - T_{\text{ref}}^2\right), \quad (\text{S15})$$

$$B_0 = \frac{\Pi}{\kappa}T_{\text{ref}} + \frac{\Pi_{\text{ref}}}{\kappa}(T - T_{\text{ref}}) - \frac{\Pi}{\kappa^2}\left(1 - \frac{\text{Si}(\pi)}{\pi}\right), \quad (\text{S16})$$

$$D_0 = \frac{3\Pi_{\text{ref}}}{\kappa^2}\left(\Pi - \frac{1}{2}\Pi_{\text{ref}}\right), \quad (\text{S17})$$

$$A_1 = \left(2T_{\text{ref}} - \frac{1}{\kappa}\right)T + \left(\frac{1}{2\kappa^2} - T_{\text{ref}}^2\right), \quad (\text{S18})$$

$$B_1 = \left(1 + \frac{4}{\pi^2}\right)\left(\frac{\Pi}{\kappa}T_{\text{ref}}\right) + \frac{\Pi_{\text{ref}}}{\kappa}(T - T_{\text{ref}}) - \frac{2\Pi}{\kappa^2}\left(\frac{1}{4} - \frac{2 + \text{Cin}(\pi)}{\pi^2}\right), \quad (\text{S19})$$

$$D_1 = \left(3 + \frac{16}{\pi}\right)\frac{\Pi_{\text{ref}}}{\kappa^2}\left(\Pi - \frac{1}{2}\Pi_{\text{ref}}\right). \quad (\text{S20})$$

From these equations,  $T = \ln Re_* / \kappa + B$  and the trigonometric integrals (Abramowitz & Stegun 1964) are defined as,

$$\text{Si}(\pi) = \int_0^\pi \frac{\sin(x)}{x} dx, \quad (\text{S21})$$

$$\text{Cin}(\pi) = \int_0^\pi \frac{\cos(x) - 1}{x} dx. \quad (\text{S22})$$

$T_{\text{ref}} = \ln Re_\tau / \kappa + B$  and  $\Pi_{\text{ref}}$  are the values at the reference condition. Specifically,  $\Pi_{\text{ref}}$  and  $B$  are set parameters matching the mean values of the streamwise velocity moments from DNS ( $\langle \widetilde{u} \rangle_{0,\text{ref}}$  and  $\langle \widetilde{u} \rangle_{1,\text{ref}}$ ), values listed in table S1,

$$\Pi_{\text{ref}} = \frac{\pi^2}{4}\kappa \left( \langle \widetilde{u} \rangle_{1,\text{ref}} - \langle \widetilde{u} \rangle_{0,\text{ref}} \right) - \frac{\pi^2}{8}, \quad (\text{S23})$$

$$B = \left( \frac{\pi^2}{4} + 1 \right) \langle \widetilde{u} \rangle_{0,\text{ref}} - \frac{\pi^2}{4} \langle \widetilde{u} \rangle_{1,\text{ref}} + \frac{1}{\kappa} \left[ \frac{\pi^2}{8} + 1 - \ln Re_\tau \right]. \quad (\text{S24})$$

The  $\langle \widetilde{u}_i \widetilde{v} \rangle_0$  term is closed by splitting the resolved and unresolved components, as done in §3,

$$\langle \widetilde{u}_i \widetilde{v} \rangle_0 = \langle \widetilde{u}_i \rangle_0 \langle \widetilde{v} \rangle_0 + \langle \widetilde{u}_i'' \widetilde{v}'' \rangle_0, \quad (\text{S25})$$

where  $\langle \widetilde{u}_i \rangle_0 = \langle U_i \rangle_0$  is known from (S2) and  $\langle \widetilde{v} \rangle_0$  is known from the right equation in (2.5). The unresolved term,  $\langle \widetilde{u}_i'' \widetilde{v}'' \rangle_0$ , is closed with an eddy viscosity approximation (with wall-normal scaling) superimposed with effects by the wake,

$$-\langle \widetilde{u}_i'' \widetilde{v}'' \rangle_0 \approx \int_0^1 \nu_{T,y} \frac{\partial U_i}{\partial y} dy + C_T (C_\Pi - 1) [\Pi e_{i,\Pi} - \Pi_{\text{ref}} e_{i,*}] \quad (\text{S26})$$

where  $\nu_{T,y}$  is an effective (dimensionless) wall-normal turbulent eddy viscosity, which is taken to be  $\nu_T \approx C_T \kappa y$ . Here,  $C_T$  is a value that is soon to be defined and  $C_\Pi$  is the tuning coefficient that controls the value of the resolved Reynolds shear stress. Using the skewed Coles profile, (S26) becomes the following,

$$-2\langle \widetilde{u}_i'' \widetilde{v}'' \rangle_0 \approx C_T [1 + (1 - C_\Pi)\Pi_{\text{ref}}] e_{i,*} + C_T [C_\Pi \Pi] e_{i,\Pi}. \quad (\text{S27})$$

At equilibrium ( $\Pi = \Pi_{\text{ref}}$  and  $e_{i,*} = e_{i,\Pi}$ ),

$$-2\langle \widetilde{u_i'' v''} \rangle_0 = C_{uv} \delta_{i1} = C_T (1 + \Pi_{\text{ref}}) \delta_{i1}, \quad (\text{S28})$$

where  $C_{uv}$  is a set parameter to control the amount of unresolved skin friction by turbulent enhancement. As a result,  $C_T = C_{uv}/(1 + \Pi_{\text{ref}})$ . Therefore, the modeled unresolved Reynolds shear stress is defined as,

$$-2\langle \widetilde{u_i'' v''} \rangle_0 \approx C_{uv} \frac{[1 + (1 - C_{\Pi})\Pi_{\text{ref}}] e_{i,*} + C_{\Pi} \Pi e_{i,\Pi}}{1 + \Pi_{\text{ref}}}, \quad (\text{S29})$$

### C. Tabulated Comparisons between TRIS and DNS

Values of the tuned parameters are listed in the first section of rows in table S1, see §B for its specific implementation into the TRIS model. For  $Re_{\tau} = 180, 395, 590$ , the DNS values of the mean streamwise velocity moments (second section of rows) and the AMI balance (fifth section of rows) were utilized in setting  $C_{uv}$ ,  $\Pi_{\text{ref}}$ , and  $B$ . In doing so, the corresponding TRIS values match the expected results within 1%. Although the AMI balance in TRIS matches within 1% of DNS, observations of figure 4 suggested further analysis on the root-mean-square. It turns out, regardless of the Reynolds number in  $180 \leq Re_{\tau} \leq 590$ , that TRIS underpredicts the root-mean-square of  $\langle \widetilde{u} \rangle_0$  and  $\langle \widetilde{w} \rangle_0$  and overpredicts  $\langle \widetilde{v} \rangle_0$ .

Regarding the DNS values of the skewness across  $180 \leq Re_{\tau} \leq 590$ ,  $S\{\langle \widetilde{u} \rangle_0\}$  is negative whereas  $S\{\langle \widetilde{v} \rangle_0\}$  is positive. This observation aligns with how sweeps and ejections generate faster and slower streamwise velocity streaks, respectively. Although TRIS generates realistic velocity structures, it does not match the DNS observation of the skewness. Furthermore, the reported excess kurtosis values of  $\langle \widetilde{u} \rangle_0$  for DNS and TRIS are both approximately Gaussian. However, the excess kurtosis of  $\langle \widetilde{v} \rangle_0$  between DNS and TRIS differ by an order of magnitude. It is evident that, from these observations, further investigation on the physics of the closure models is required in order to refine the accuracy of TRIS to match higher-order statistics.

A strong trait that TRIS possesses is the ability to successfully run at high Reynolds number flows ( $1000 \leq Re_{\tau} \leq 10^6$ ). Note that DNS data of the open-channel flow at this range of Reynolds numbers are not available. At an arbitrarily high  $Re_{\tau}$ ,  $C_{uv} = 0.625$  is set according to the estimate made through the purple dashed lines in figure 2. Additionally, since the highest Reynolds number ran by DNS is  $Re_{\tau} = 590$  for the open-channel flow,  $\Pi_{\text{ref}} = 0.162$  and  $B = 5.07$  are set for the higher Reynolds number simulations. Consequently, this leaves  $C_{\Pi} = 1.68$  to be tuned to match the resolved skin friction enhancement (red dashed line in figure 2) in the AMI balance. According to the observations made at the lower Reynolds number flows ( $Re_{\tau} = 180, 395, 590$ ), it is expected that the statistical values of (at least) the root-mean-square, skewness, and excess kurtosis of the TRIS simulations at  $Re_{\tau} = 1000, 5200, 10^6$  would deviate from a true physical baseline.

### REFERENCES

- ABRAMOWITZ, MILTON & STEGUN, IRENE A., ed. 1964 *Handbook of Mathematical Functions with Formulas, Graphs, and Mathematical Tables, Applied Mathematics Series*, vol. 55. Washington, D.C.: U.S. Department of Commerce, National Bureau of Standards.
- GRAHAM, J., KANOV, K., YANG, X. I. A., LEE, M., MALAYA, N., LALESCU, C. C., BURNS, R., EYINK, G., SZALAY, A., MOSER, R. D. & MENEVEAU, C. 2016 A web services accessible database of turbulent channel flow and its use for testing a new integral wall model for les. *JoT* **17** (2), 181–215.
- LEE, M. & MOSER, R. D. 2015 Direct numerical simulation of turbulent channel flow up to  $Re_{\tau} = 5200$ . *J. Fluid Mech.* **774**, 395–415.

Table S1: Tuning parameters (implemented in §B) for TRIS and statistics of the velocity moments: mean ( $\bar{\phi}$ ), root-mean-square ( $\text{RMS}\{\phi\}$ ), skewness ( $S\{\phi\}$ ), and kurtosis ( $K\{\phi\}$ ) are listed in descending order. The last section of rows list the AMI balance (values also illustrated in figure 2). DNS data is available up to  $Re_\tau = 590$  while TRIS data is up to  $Re_\tau = 10^6$ .

$Re_\tau$	180		395		590		1000	5200	$10^6$
Simulation	DNS	TRIS	DNS	TRIS	DNS	TRIS	TRIS	TRIS	TRIS
$C_\Pi$	-	5.93	-	2.68	-	2.25	1.92	1.69	1.68
$C_{uv}$	-	0.407	-	0.540	-	0.563	0.600	0.625	0.625
$\Pi_{\text{ref}}$	-	0.344	-	0.203	-	0.162	0.162	0.162	0.162
$B$	-	4.68	-	4.97	-	5.07	5.07	5.07	5.07
$\overline{\langle \tilde{u} \rangle_0}$	15.7	15.6	17.6	17.5	18.6	18.5	19.8	23.8	36.6
$\overline{\langle \tilde{u} \rangle_1}$	17.3	17.2	19.0	18.9	20.0	19.9	21.2	25.2	38.0
$\text{RMS}\{\langle \tilde{u} \rangle_0\}$	0.87	0.50	0.84	0.48	0.88	0.46	0.46	0.47	0.48
$\text{RMS}\{\langle \tilde{v} \rangle_0\}$	0.38	0.72	0.37	0.71	0.36	0.76	0.74	0.78	0.80
$\text{RMS}\{\langle \tilde{w} \rangle_0\}$	0.35	0.22	0.34	0.17	0.33	0.15	0.15	0.15	0.15
$S\{\langle \tilde{u} \rangle_0\}$	-0.14	0.21	-0.16	0.039	-0.19	0.011	0.019	0.043	0.050
$S\{\langle \tilde{v} \rangle_0\}$	0.22	-0.18	0.16	-0.59	0.18	-0.79	-0.73	-0.68	-0.64
$K\{\langle \tilde{u} \rangle_0\}$	-0.19	-0.050	-0.19	-0.23	-0.23	-0.31	-0.28	-0.26	-0.25
$K\{\langle \tilde{v} \rangle_0\}$	0.095	1.4	0.022	1.7	0.040	1.7	1.6	1.4	1.2
$C_{f,\text{res}}/C_f$	0.388	0.381	0.356	0.357	0.365	0.370	0.353	0.361	0.369
$C_{f,\text{unres}}/C_f$	0.407	0.409	0.542	0.539	0.563	0.558	0.602	0.628	0.631
$C_{f,\text{lam}}/C_f$	0.205	0.210	0.102	0.104	0.072	0.072	0.045	0.010	0.000

LOZANO-DURÁN, A., HACK, M. J. P. & MOIN, P. 2018 Modeling boundary-layer transition in direct and large-eddy simulations using parabolized stability equations. *Phys. Rev. Fluids* **3**, 023901.

MOSER, R. D., KIM, J. & MANSOUR, N. N 1999 Direct numerical simulation of turbulent channel flow up to  $Re_\tau = 590$ . *Phys. Fluids* **11** (4), 943–945.

ROSS, S.M. 1998 *A First Course in Probability*. Prentice Hall.

SHIRIAN, YASAMAN, HORWITZ, JEREMY A.K. & MANI, ALI 2023 On the convergence of statistics in simulations of stationary incompressible turbulent flows. *Comput. Fluids* **266**, 106046.